Modeling of Dual-Phase Composite Magnetic Material and Its Application in Transformers

Yang Liu [1,2]**, Fuyao Yang** [1,2]**, Yu Han** [1,2,*]**, Jie Gao** [1,2]**, Dezhi Chen** [3] **and Haonan Bai** [3]

1   State Key Laboratory of Advanced Power Transmission Technology, Beijing 102209, China; liuyang365@163.com (Y.L.); gaojie2324@163.com (J.G.)
2   State Grid Smart Grid Research Institute Co., Ltd., Beijing 102209, China
3   School of Electrical Engineering, Shenyang University of Technology, Shenyang 110870, China; chendezhi@sut.edu.cn (D.C.); baihaonan@smail.sut.edu.cn (H.B.)
*   Correspondence: hanyu2026@163.com

Abstract: Dual-phase composite magnetic materials have magnetic and permanent magnetic properties. They can realize the dual-phase conversion of soft magnetic and permanent magnetic composites with a small amount of excitation energy. They have the advantages of good control and conversion characteristics and save energy, and they have a wide range of application scenarios in regard to power equipment. In this paper, the magnetization modeling of dual-phase composite magnetic materials is carried out based on micromagnetic theory, and a specific mathematical expression is given. Secondly, the preparation process of the dual-phase composite magnetic material is studied, the dual-phase composite magnetic material is prepared, and the demagnetization curve of the dual-phase composite magnetic material is measured. Finally, the application of dual-phase composite magnetic materials in power equipment is carried out. Using the soft magnetic and permanent magnetic characteristics of dual-phase composite magnetic materials, their impact on DC bias suppression in transformers is assessed. Magnetic circuit reluctance theory is used to develop the structure and electromagnetic design of a transformer. A transformer prototype with DC bias suppression ability based on dual-phase composite magnetic materials is manufactured, and simulation and experimental research are carried out. The simulation and experimental results verify the correctness of the proposed scheme. Although this scheme requires a more complex core structure, the energy-saving effect is remarkable without changing the transformer's neutral grounding. The indicators meet the actual requirements of the project.

Keywords: dual-phase magnetic material; compensation; power transformer; DC bias; structural design; electromagnetic design

1. Introduction

Dual-phase composite magnetic materials have magnetic and permanent magnetic properties. They can realize the dual-phase conversion of soft magnetic and permanent magnetic composites with a small amount of excitation energy. They have the advantages of good control and conversion characteristics and save energy, and they have a wide range of application scenarios in regard to power equipment [1–4].

The DC bias phenomenon in transformers, caused by HVDC and geomagnetic storms, can seriously affect the security and stable operation of the power system [5]. Consequently, researchers have paid attention to DC bias compensation technology [6–8]. In [9], a DC current-blocking device for transformer neutrals is developed. In [10], an investigation was conducted to reduce the flow of geomagnetically induced currents (GICs) via power transformers. This was achieved by implementing an AC grounding channel using a capacitor between the earth or ground and the neutral point of a power transformer, but only when the GIC was identified. In [11], when designing a DC bias device for transformers, it was found that thoroughly evaluating both the resistance and the withstand
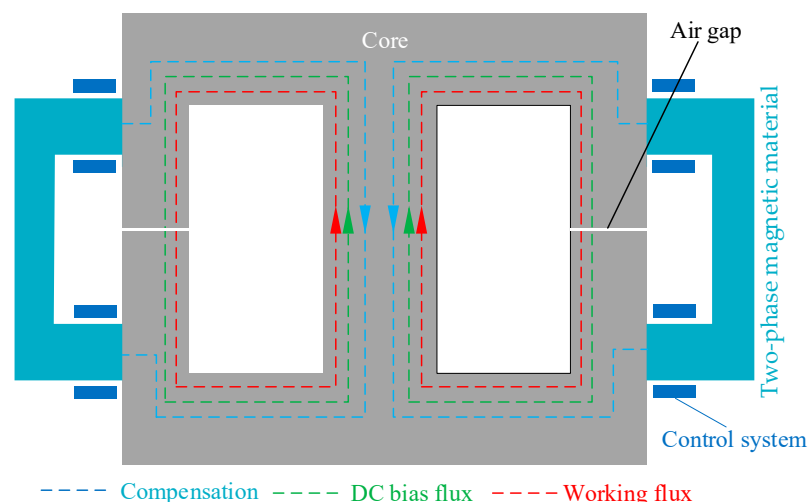
voltage was important. To ensure the safe operation of the transformer when the fault zero-sequence current was high, choosing a lower resistance was recommended whenever possible. In [12], an optimal study was conducted on the DC current-blocking technique using the existing dual protection topology. The selection and design parameters for the device were determined based on applicable concepts. In [9–12], the DC bias was suppressed by calculating and installing series capacitors or resistors, but this method will raise the neutral point potential of the transformer and may cause DC bias in other transformers. Neutral point compensation technology can suppress the grounding current [13]. However, according to a large number of previous studies, this compensation method has some limitations; for example, the real-time estimation of the injected current is imprecise, leading to inadequate compensation and overcompensation [14,15]. Utilizing the auxiliary windings of hybrid transformers can achieve full compensation of the core DC bias through the establishment of a modulation compensation current [16]. However, the increased size of the compensation coil may affect the normal operation of the transformer.

The existence of DC bias in power transformers seriously affects the power quality and normal operation of the equipment [16–18]. Therefore, DC bias has increasingly become the focus of research by scholars [19–25]. The main compensation technologies are used to connect the resistance with the neutral point, connect the capacitance, reverse the electric potential compensation, install the wound degaussing coil in the transformer core, and so on. However, these methods have drawbacks that pose a great threat to the security of power systems. Currently, devising effective measures to suppress the influence of DC bias in transformer design remains a challenge.

This research analyzed and completed the calculations for the preparation of dual-phase magnetic material, the structural and electromagnetic design of a new power transformer, and the control system, comprehensively starting from the design stage and the dual-phase magnetic conversion mechanism. It provides an effective method, reference, and technical means for manufacturing the new power transformer with a DC bias compensation function. The simulation and experimental results show that the compensation effect of the transformer on DC bias is evident. The results verify the correctness and feasibility of the scheme.

2. Modeling of Dual-Phase Composite Magnetic Materials

Figure 1 displays a structural schematic diagram of the new power transformer. The control system transfers the magnetic flux to the dual-phase magnetic material when DC bias is detected. The supplemented magnetic flux is equal to the DC bias magnetic flux but in the opposite direction. When the DC bias disappears, the control system demagnetizes the dual-phase magnetic material. The transformer returns to its normal state.

Figure 1. Structure schematic diagram of the new power transformer.

3. The Establishment of the Dual-Phase Magnetic Hysteresis Mathematical Model and the Research of the Preparation of Material

3.1. Micromagnetic Modeling of Dual-Phase Magnetic Materials

Due to the lack of consideration of magnetic material properties under mechanical stress conditions in this article, magnetoelasticity is not considered. In the theory of micromagnetics, when the magnetoelastic property is neglected, the total Gibbs free energy of any magnet can be expressed as:

$$E_{tot} = E_{ex} + E_{an} + E_d + E_{\mathrm{ap}} \tag{1}$$

where E_{ex} is the exchange interaction energy; E_{an} is magnetocrystalline anisotropy; E_d is demagnetization energy; and E_{ap} is saimanneng.

(1) Exchange energy

The exchange interaction energy refers to the electrostatic interaction energy between two adjacent atoms. For substances with strong magnetism, the magnetic moments of adjacent atoms are orderly arranged due to the existence of the exchange interaction energy. The pure quantum effect caused by the Coulomb force between atoms is the source of the exchange coupling of adjacent lattice points. Exchange interaction is a short-range force, so only the nearest-neighbor interaction is considered. According to Heisenberg's exchange theory, the exchange energy between two nearest spin atoms is:

$$\varepsilon_{ex} = -2J_{ij}\vec{S_i}\cdot\vec{S_j} \tag{2}$$

where the *i* atomic spin angular momentum is $\vec{S_i}$, the *j* atomic spin angular momentum is $\vec{S_j}$, and J_{ij} is the exchange integral constant.

In addition, it is generally believed that the angle φ_{ij} between the spin magnetic moments $\vec{S_i}$ and $\vec{S_j}$ of the adjacent ferromagnetic atoms is very small, so:

$$\vec{S_i}\cdot\vec{S_j} = S^2\cos\varphi_{ij} \approx S^2(1 - \frac{1}{2}{\varphi_{ij}}^2) \tag{3}$$

$$\varepsilon_{ex} = -JS^2\sum\cos\varphi_{jj} \tag{4}$$

If the exchange interaction is zero when all spins are parallel, then the exchange interaction energy when spins are not parallel is expressed as:

$$\varepsilon_{ex} = -JS^2\sum(1 - \cos\varphi_{ij}) = JS\sum\varphi_{ij}^2 \tag{5}$$

$$\varphi_{ij} = \left|\vec{m_i} - \vec{m_j}\right| \tag{6}$$

where $\vec{m_i}$ and $\vec{m_j}$ is the $\vec{S_j}$ unit magnetization vector associated with $\vec{S_i}$, $\vec{m} = \vec{M}/|M_s|$. $\vec{r_{ij}}$ is used to express the position vector from atom *i* to atom *j*. $\left|\vec{m_i} - \vec{m_j}\right|$ is expanded to the first term of Taylor series, then:

$$\left|\vec{m_i} - \vec{m_j}\right| = \left|(\vec{r_{ij}}\cdot\nabla)\vec{m}\right| \tag{7}$$

Finally, the exchange density is:

$$\varepsilon_{ex} = JS^2\sum_i\sum_{ij}[\vec{r_{ij}}\cdot\nabla\vec{m}]^2 \tag{8}$$

If the sum is replaced by an integral, the exchange energy density of cubic crystal is:

$$\varepsilon_{ex} = \frac{1}{2}\int C[(\nabla m_x)^2 + (\nabla m_y)^2 + (\nabla m_z)^2]d\tau \tag{9}$$

where $C = \frac{2JS^2}{a}C'$, $C'\alpha$ is the lattice constant, and the values are 1, 2, and 4 for simple cubic, body-centered cubic, and face-centered cubic, respectively. For the dense hexagonal crystal system, the expression of the above enlightenment energy is also valid. The exchange energy constant C is expressed as $C = \frac{4\sqrt{2}JS^2}{a}C'\alpha$, where α refers to the distance between the nearest atoms.

When $A = C/2$, the total exchange energy can be expressed as:

$$E_{ex} = \int A[(\nabla m_x)^2 + (\nabla m_x)^2 + (\nabla m_x)^2]dV \tag{10}$$

(2)　Zeeman energy

Zeeman energy refers to the energy generated by the magnet under the action of an external field $\vec{H}_{ap}$, expressed as:

$$E_{\alpha p} = \int_\Omega \mu_0 \vec{M} \cdot \vec{H}_{ap} dV \tag{11}$$

(3)　Magnetocrystalline anisotropy

Anisotropy energy generally includes magnetocrystalline anisotropy, surface anisotropy, shape anisotropy, and anisotropy energy caused by magnetoelasticity. In general, in micromagnetic calculations, only magnetocrystalline anisotropy is considered, and it is introduced in this paper. Magnetic-crystal anisotropy is the energy that varies with the direction of the magnetization vector. Magnetic crystal anisotropy is usually very small compared with exchange energy, but the direction of the magnetic moment is determined by anisotropy. The magnetic anisotropy properties exhibit a symmetry relationship with the crystal structure of the material. Therefore, based on the crystal symmetry, magnetic crystal anisotropy can be expressed in a phenomenological form.

For a cubic crystal system, the density of magnetocrystalline anisotropy can be expressed as follows [26]:

$$\varepsilon_{an} = K_1(a_1^2 a_2^2 + a_3^2 a_2^2 + a_1^2 a_3^2) + K_2 a_1^2 a_2^2 a_3^2 + K_3(a_1^2 a_2^2 + a_3^2 a_2^2 + a_1^2 a_3^2)^2 + \cdots \tag{12}$$

In the above formula, a_1, a_2, and a_3 are the $\vec{M}$ directional cosine of the saturation magnetization vector and the rectangular coordinate system; K_1, K_2, and K_3 represent the anisotropy constants of the magnetic crystal of the cubic crystal system, which represent the degree of the magnetic crystal anisotropy.

Order: $a_2 = m_y$, $a_1 = m_x$, $\vec{m} = \vec{M}/M_s$, $a_3 = m_z$; therefore:

$$\varepsilon_{an} = K_1(m_x^2 m_y^2 + m_x^2 m_z^2 + m_z^2 m_y^2) + K_2 m_x^2 m_y^2 m_z + \cdots \tag{13}$$

Generally, K_2 is smaller than K_1, so it can be ignored. For example, for Fe, $K_1 > 0$.

The easily magnetized axis is (100); when $K_1 < 0$, the direction of the easily magnetized axis is (111), such as *Ni* (nickel). The density of the magnetocrystalline anisotropy of uniaxial crystals can be expressed as:

$$\varepsilon_{an} = K_1 \sin^2 \theta + K_2 \sin^4 \theta + \cdots \tag{14}$$

where θ is the included angle between the magnetization vector $\vec{M}$ and the axis of the magnetizable axis C. K_1 and K_2, respectively, represent the corresponding anisotropy constants of the magnetic crystal, and the above formula can also be expressed as:

$$\varepsilon_{an} = K_1[1 - (\vec{e} \cdot \vec{m})^2] + K_2[1 - (\vec{e} \cdot \vec{m})^2]^2 \tag{15}$$

where $\vec{e}$ is the unit vector in the direction of the magnetizable axis. When $K_1 < 0$, $K_1 > 0$, and the easy-magnetized axis is on the base plane. The concept of the anisotropic field is often used to describe the anisotropic properties of magnetic crystals, which is defined as:

$$\varepsilon_{an} = -\mu_0 \vec{H}_{an} \cdot \vec{M} \tag{16}$$

For cubic crystals, the anisotropic field is expressed as:

$$\vec{H}_{\alpha n}(100) = \frac{2K_1}{\mu_0 M_s} \tag{17}$$

For cubic $\vec{H}_{\alpha n}(111) = \frac{4K_1}{3\mu_0 M_s}$ crystal, K_1 when it is $\vec{M}$ along the (111) direction, for uniaxial crystal $\vec{H}_{\alpha n} = \frac{2(K_1+K_2)}{\mu_0 M_s}$. In most cases, K_2 is much smaller than K_1, and $\vec{H}_{\alpha n} = \frac{2K_1}{\mu_0 M_s}$. The total magnetocrystalline anisotropy is:

$$E_{an} = \int_\Omega \varepsilon_{an} dV \tag{18}$$

(4)   Demagnetization energy

Demagnetization energy originates from the interaction between classical magnetic dipoles and contributes to the stable existence of magnetic domains. Demagnetization energy is also known as static magnetic energy. In comparison, the calculation of demagnetization energy is relatively complicated and time-consuming. Solving the demagnetization problem is crucial in micromagnetism. The demagnetizing field can be calculated by magnetic scalar potential or magnetic vector potential. This paper simply introduces the method of magnetic scalar potential. The demagnetization field can be expressed as:

$$\vec{H}_d(\vec{r}) = \frac{1}{4\pi} \int_\Omega \left[\vec{M}(\vec{r'}) \left[\frac{3(\vec{r} - \vec{r'})(\vec{r} - \vec{r'})}{\left| \vec{r} - \vec{r'} \right|^5} - \frac{1}{\left| \vec{r} - \vec{r'} \right|^3} \right] \right] dV' \tag{19}$$

Demagnetization energy is expressed as:

$$E_d = -\frac{1}{2} \int_\Omega \mu_0 \vec{M} \cdot \vec{H}_d dV \tag{20}$$

The demagnetization energy is determined by both $\nabla \times \vec{H}_d = 0$ and $\nabla \times \vec{B} = 0$, and:

$$\vec{B} = \mu_0 (\vec{M} + \vec{H}_d) \tag{21}$$

Because the magnetic field of the vortex is 0, which means the $\vec{H}_d$ irrotational property, the magnetic scale potential is introduced:

$$\vec{H}_d = -\nabla U \tag{22}$$

Then, the magnetic scale potential U satisfies the following equation:

$$\nabla^2 U_{in} = \nabla \vec{M} \tag{23}$$

$$\nabla^2 U_{out} = 0 \tag{24}$$

According to the boundary conditions of $\vec{B}$ and $\vec{H_d}$:

$$\vec{n} \cdot (\vec{B_2} - \vec{B_1}) = 0 \tag{25}$$

$$\vec{n} \times (\vec{H_{d2}} - \vec{H_{d1}}) = 0 \tag{26}$$

where $\vec{n}$ is the normal unit vector from medium 1 to medium 2. The boundary conditions of U are:

$$\begin{cases} U_{in} = U_{out} \\ \frac{\partial U_{in}}{\partial n} - \frac{\partial U_{out}}{\partial n} = \vec{M} \cdot \vec{n} \end{cases} \tag{27}$$

where $\vec{n}$ is the normal unit vector from the inside of the magnet to the outside of the magnet. In addition, when $r \to \infty$, $|rU|$ and $|r^2 \nabla U|$ are limited. According to the uniqueness theorem, the U solution satisfying the above equations and boundary conditions is unique, and the general solution of $\vec{H_d}$ and U can be obtained as follows:

$$\vec{H_d}(\vec{r}) = -\frac{1}{4\pi} \int_{\Omega} \frac{(\vec{r} - \vec{r'}) \nabla \cdot \vec{M}(\vec{r'})}{\left|\vec{r} - \vec{r'}\right|^3} dV' + \frac{1}{4\pi} \int_{\partial\Omega} \frac{(\vec{r} - \vec{r'}) \vec{n} \cdot \vec{M}(\vec{r'})}{\left|\vec{r} - \vec{r'}\right|^3} dS' \tag{28}$$

$$U(\vec{r}) = -\frac{1}{4\pi} \int_{\Omega} \frac{\nabla \cdot \vec{M}(\vec{r'})}{\left|\vec{r} - \vec{r'}\right|^3} dV' + \frac{1}{4\pi} \int_{\partial\Omega} \frac{\vec{n} \cdot \vec{M}(\vec{r'})}{\left|\vec{r} - \vec{r'}\right|^3} dS' \tag{29}$$

Due to the surface magnetic charge $\sigma_m = -\vec{n} \cdot \vec{M}(\vec{r})$ and magnetic charge volume $\rho_m = -\vec{n} \cdot \vec{M}(\vec{r})$, the demagnetization field and magnetic scalar potential are expressed as follows:

$$\vec{H_d} = -\frac{1}{4\pi} \int_{\Omega} \frac{(\vec{r} - \vec{r'}) \rho_m(\vec{r'})}{\left|\vec{r} - \vec{r'}\right|^3} dV' + \frac{1}{4\pi} \int_{\partial\Omega} \frac{(\vec{r} - \vec{r'}) \sigma_m(\vec{r'})}{\left|\vec{r} - \vec{r'}\right|^3} dS' \tag{30}$$

$$U(\vec{r}) = -\frac{1}{4\pi} \int_{\Omega} \frac{\rho_m(\vec{r'})}{\left|\vec{r} - \vec{r'}\right|^3} dV' + \frac{1}{4\pi} \int_{\partial\Omega} \frac{\sigma_m(\vec{r'})}{\left|\vec{r} - \vec{r'}\right|^3} dS' \tag{31}$$

From (30)–(31), the demagnetization field is the combination of the demagnetization field resulting from the surface magnetic charge and the body magnetic charge. Demagnetization energy can also be expressed as:

$$E_d = \frac{1}{2}\mu_0 \int_{\Omega} \rho_m(\vec{r}) U(\vec{r}) dV + \frac{1}{2}\mu_0 \int_{\partial\Omega} \sigma_m(\vec{r}) U(\vec{r}) dS \tag{32}$$

Equation (32) is the expression of demagnetization field and demagnetization energy, but it is difficult to complete such a large amount of calculation on an ordinarily configured computer. In view of this, researchers have adopted other acceleration methods to solve this problem, mainly the Hierarchical Calculation method and the Fast Fourier Transform method, which greatly improve the calculational speed.

3.2. Static and Dynamic Methods

(1)   Static calculation method

When the Gibbs free energy of the magnet is taken as a minimum, the equilibrium distribution of the magnetization vector can be obtained. The static micromagnetics calculation is based on the equilibrium condition of taking the minimum value from E_{tot} or the condition that E_{tot}'s variation is 0, and the Brown equation can be obtained:

$$\begin{cases} \vec{m} \times \left[2A \dfrac{\partial \vec{m}}{\partial \vec{n}} + K_s \left(\vec{n} \cdot \vec{m} \right) \vec{n} \right] = 0 \\ \vec{m} \times \left[2A \nabla^2 \vec{m} + \mu_0 M_s \left(H_{op} + H_d \right) - \dfrac{\partial \vec{\omega_{an}}}{\partial \vec{m}} \right] = 0 \end{cases} \tag{33}$$

When surface anisotropy is ignored, the boundary condition can be expressed as:

$$\frac{\partial \vec{m}}{\partial \vec{n}} = \vec{n} \cdot \left(\nabla \vec{m} \right) = 0 \tag{34}$$

where the concept of effective field $\vec{H}_{eff}$ is cited. Field effectiveness $\vec{H}_{eff}$ is described as the variation in free energy, which provides the actual moment acting on the magnetization vector.

$$\begin{aligned} H_{eff} &= -\frac{1}{\mu_0 M_s} \frac{\partial E_{tot}}{\partial \vec{m}} = -\frac{1}{\mu_0 M_s} \frac{\partial E_{ex}}{\partial \vec{m}} - \frac{1}{\mu_0 M_s} \frac{\partial E_{an}}{\partial \vec{m}} - \frac{1}{\mu_0 M_s} \frac{\partial E_{ap}}{\partial \vec{m}} - \frac{1}{\mu_0 M_s} \frac{\partial E_d}{\partial \vec{m}} \\ &= \vec{H}_{ex} + \vec{H}_{ap} + \vec{H}_d + \vec{H}_{an} \end{aligned} \tag{35}$$

Brown's equation is written as:

$$\mu_0 M_s \vec{m} \times \vec{H}_{eff} = 0 \tag{36}$$

When the energy is very small, the directions of $\vec{H}_{eff}$ and $\vec{m}$ in the corresponding magnet are the same everywhere. The static micromagnetics calculation directly minimizes the energy according to the above principle, thus obtaining the distribution of the magnetization vector in the equilibrium state.

(2)   Dynamic calculation method

The expression of the total free energy of the magnet is written as (37):

$$E_{tot} = E_{ex} + E_d + E_{an} + E_H \tag{37}$$

When the system is under a changing external field, the dynamic equation of the magnetic moment must be considered, which follows the Landau–Lifshitz–Gilbert (LLG) dynamic equation:

$$\frac{dM}{dt} = -\frac{\omega}{1+a^2} M \times H_{eff} - \frac{a\omega}{(1+a^2)M_s} M \times (M \times H_{eff}) \tag{38}$$

where M is the magnetization vector, α is the damping coefficient, ω is the rotational magnetic ratio, and the effective field $\vec{H}_{eff}$ is defined as the variation in free energy, $\vec{H}_{eff} = -\frac{1}{\mu_0} \frac{\partial E_{tot}}{\partial \vec{M}}$, which provides the actual torque acting on the magnetization vector.
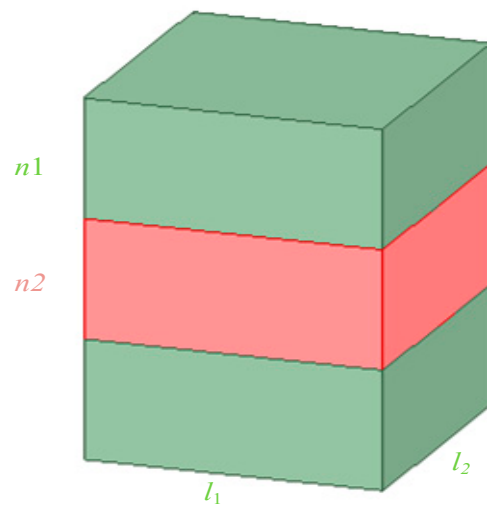
A small change in each magnetic moment in the system will cause a change in the energy state of the whole system. In other words, the dynamic equation of each magnetic moment is closely related, so the system will get the minimum energy, which is also the criterion for whether the calculation can be terminated. The boundary condition of the dynamic equation is the same as the static boundary condition, that is, when surface anisotropy is ignored, and the boundary condition is:

$$\frac{\partial \vec{m}}{\partial n} = 0 \tag{39}$$

The dynamic micromagnetic calculation solves the above Gilbert or Landau–Lifshitz dynamic equation and then obtains the image of the magnetization vector moving with time.

3.3. Hysteresis Characteristics of Nanocomposite Magnetic Materials

This paper is based on the theory of micromagnetism, employing a three-dimensional dynamic model, and the dynamic calculation method of micromagnetism is used to calculate $Nd_2Fe_{14}B/\alpha$-$Fe/Nd_2Fe_{14}B$ on the OOMMF 2.0 (beta) software platform. The magnetization process of $Nd_2Fe_{14}B$ exchange-coupled magnetic three-layer film is simulated, and the hysteresis loops of nano-phase composite $Nd_2Fe_{14}B$ three-layer film under different soft magnetic layer thickness and the relationship curve between soft magnetic layer thickness and coercivity are calculated. The three-layer film model is shown in Figure 2. n1 represents the thickness of the rigid magnetic stratum, n2 represents the thickness of the soft magnetic layer, and l_1 and l_2, respectively, represent the width and length of the three-layer film model.

Figure 2. Calculation model of nanometer dual-phase three-layer film.

In the model calculated in this paper $l_1 = l_2 = 300$ nm, along the Z-axis, the external magnetic field is directed. The length and width of the split unit are 10 nm, and the height is 1 nm. The calculation parameters of the nano-phase composite $Nd_2Fe_{14}B$ three-layer film are shown in Table 1.

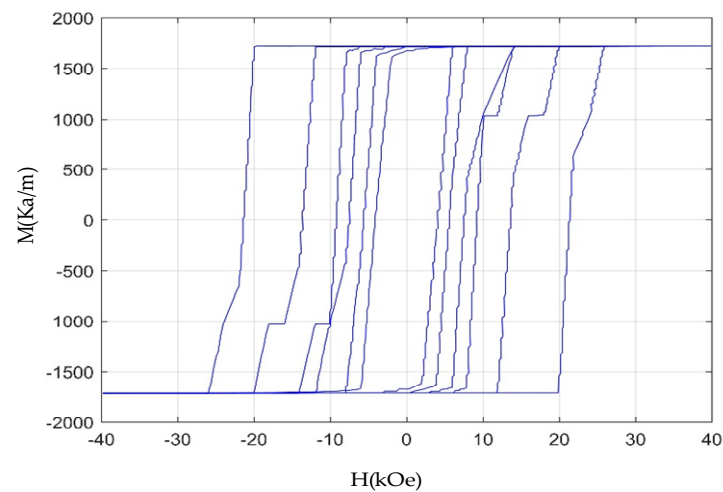**Table 1.** Parameters of nano-phase composite $Nd_2Fe_{14}B$ three-layer film.

Item	Saturated Magnetization (kA/m)	Anisotropic Constant (MJ/m^3)	Exchange Coupling Constant (J/m)
Hard magnetic layer	1288	4.3	7.7×10^{-12}
Soft magnetosphere	1720	0.046	2.5×10^{-11}

In this paper, when the hard magnetic layer is 5 nm thick, the calculation of the soft magnetic layer is in the range of 1 nm to 20 nm, and the hysteresis loops under different soft magnetic layer thicknesses are obtained, as shown in Figure 3. The relationship curve between the coercivity and the soft magnetic layer thickness is obtained, as shown in Figure 4.
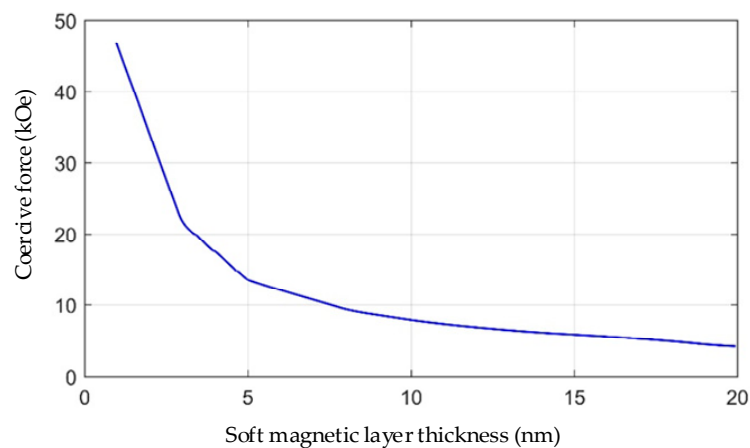
The relationship between the microscopic parameters and the macroscopic magnetic properties of the nanocomposite magnetic materials was established by using the micromagnetic theory and the OOMMF software platform to calculate the hysteresis properties of the nanocomposite magnetic materials. In this project, the microscopic parameters of the nanocomposite magnetic materials closest to the magnetic properties can be obtained

according to the requirements of the material properties, which can be used to determine the preparation of the materials.

Figure 3. Nano-phase composite $Nd_2Fe_{14}B$ hysteresis loop family.

Figure 4. Relationship curve between soft magnetic layer thickness and coercivity.

3.4. Research of the Influence of Element Composition and Heat Treatment Craft on the Dual-Phase Magnetic Material

Based on the above analysis, the remanence, coercivity, and hysteresis loop are defined. In order to manufacture the dual-phase magnetic material, the influence of elements and heat treatment craft to the dual-phase magnetic material are discussed below.

(1) Influence of Element Composition on the Dual-phase Magnetic Material

The chemical formula for the dual-phase magnetic material is Fe-12Co-24Cr. The influence of the contents of the element on the dual-phase magnetic material is significant. A higher content of Co alloy leads to better magnetic performance. However, its workability is poor. If the content of the Co alloy is low, its workability is good, but the craft is complex and difficult to control. The adjustment range of the magnetic parameter will be narrow. The content fluctuation of the Cr will affect the coercivity of the material. Studies have shown that if the fluctuation of Cr is 3%, the fluctuation of coercivity will be 40%.

(2) Influence of Heat Treatment Craft on the Dual-phase Magnetic Material

The heat treatment craft is closely related to the magnetic performance of the material. Temperature control has a significant impact on both the strong magnetic phase and the

weak magnetic phase. Based on a large number of experiments, the five-rank tempering craft was adopted. The implementation process is listed as follows:

$$620\,^{\circ}\text{C} \times 1\,\text{h} + 610\,^{\circ}\text{C} \times 1\,\text{h} + 590\,^{\circ}\text{C} \times 2\,\text{h} + 570\,^{\circ}\text{C} \times 3\,\text{h} + 560\,^{\circ}\text{C} \times 3\,\text{h}.$$

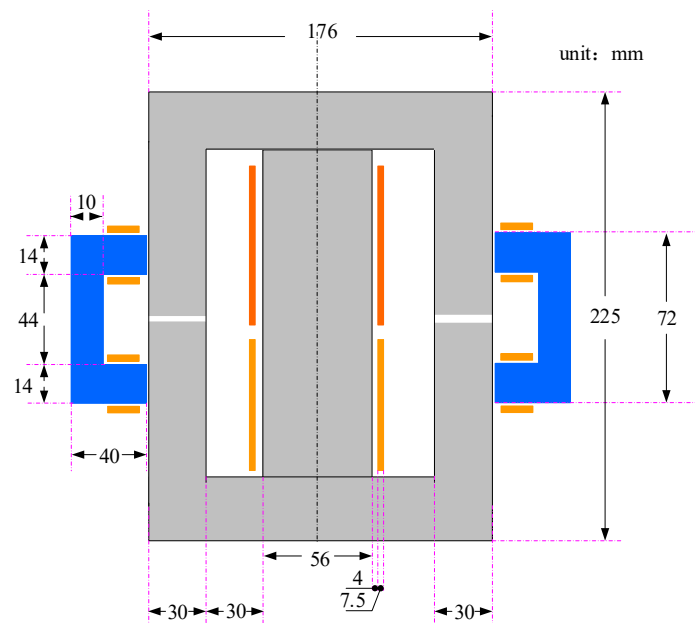(3)   Preparation of the Dual-phase Magnetic Material

Based on the above analysis, the dual-phase magnetic material can be prepared. Figure 5 shows the sample of the dual-phase magnetic material.

Figure 5. Demonstration of the dual-phase magnetic material.

4. Structure Design of the New Power Transformer

According to the latest research results on dual-phase magnetic material, a more reasonable solution is to utilize the materials on both sides of the new power transformer adjacent to the column in order to achieve DC bias compensation. The equivalent magnetic circuit of the new power transformer was analyzed based on the reluctance theory under the condition of the DC magnetic potential, and the AC magnetic potential was considered, respectively. Figure 6 shows the structure of the new transformer.

Figure 6. Structure of the new transformer.

The equivalent magnetic circuit of the new power transformer is shown in Figure 7. $(IN)_{AC}$ represents the AC potential, $(IN)_{DC}$ represents the DC potential, and $(IN)_{Magnet}$ represents the compensation magnetic potential.
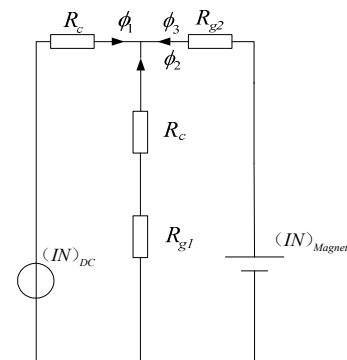
Figure 7. Equivalent magnetic circuit model.

Figure 8 shows the equivalent magnetic circuit of the new power transformer under the condition of considering the DC flux only. Equation (40) can be obtained based on Kirchhoff's voltage and current laws.

$$\begin{cases} (IN)_{DC} = \phi_1[R_c + (R_c + R_{g1})//R_{g2}] \\ (IN)_{Magnet} = \phi_2[R_{g2} + (R_c + R_{g1})//R_c] \\ \phi_1 + \phi_2 + \phi_3 = 0 \end{cases} \tag{40}$$

where R_c is the reluctance of the silicon steel, and ϕ_1 and ϕ_3 are the DC flux. The DC flux is not expected to flow to the adjacent column, so ϕ_2 is set to zero. R_{g1} and R_{g2} can be obtained. That is to say, the gap can be obtained.
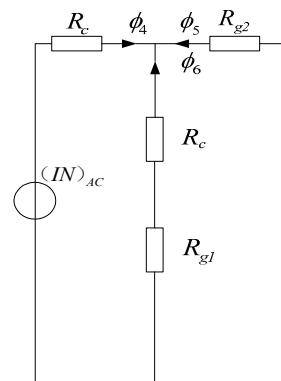
Figure 8. Equivalent magnetic circuit model considering DC flux only.

Figure 9 shows the equivalent magnetic circuit of the new power transformer under the condition of considering the AC flux only. Equation (41) can be obtained based on Kirchhoff's voltage and current laws.

$$\begin{cases} (IN)_{AC} = \phi_4[R_c + (R_c + R_{g1})//R_{g2}] \\ \phi_5 R_{g2} = \phi_6(R_c + R_{g1}) \\ \phi_4 + \phi_5 + \phi_6 = 0 \end{cases} \tag{41}$$

where R_c is the reluctance of the silicon steel, and ϕ_5 and ϕ_6 are the AC flux. The AC flux is not expected to flow the dual-phase magnetic material, so ϕ_4 is set to zero. R_{g1} and R_{g2} can be obtained. That is to say, the gap can be obtained. According to (40) and (41), the gap length of the 220 V/110 V/2 kVA new transformer is shown in Table 2. Figure 10 shows the prepared model.

Figure 9. Equivalent magnetic circuit model considering AC flux only.

Table 2. Types sizes of the new transformer.

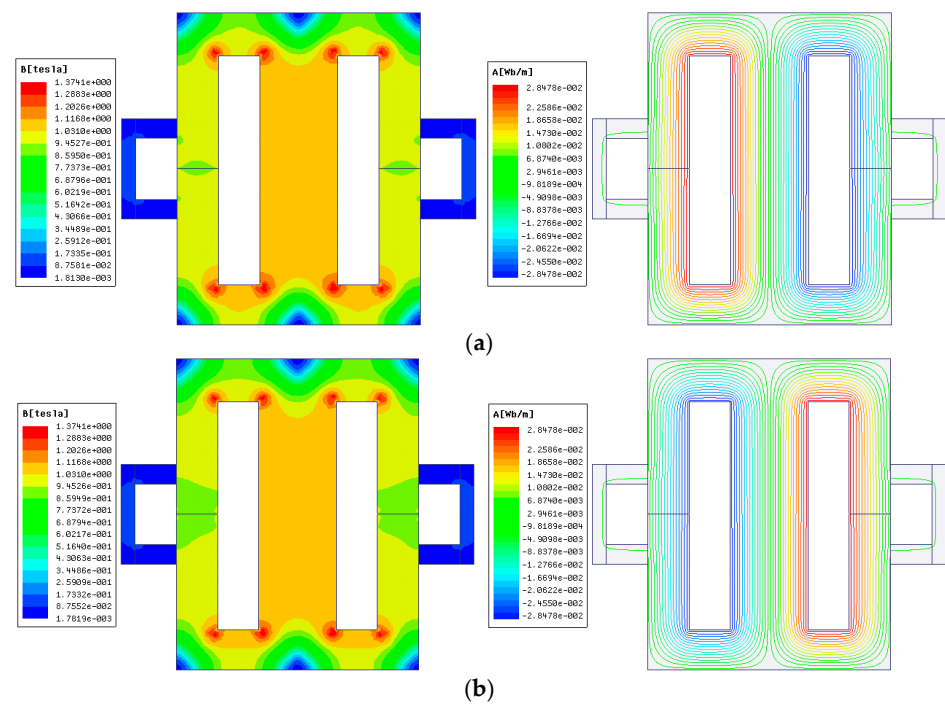| Transformer Type	gap1 (mm)	gap2 (mm)	Length of the Material Magnetic Circuit (mm)
220 V/110 V/2 kVA	0.3–0.7	0.1–0.4	128

Figure 10. Prototype of the new transformer.

5. Simulation and Experimental Study on the New Transformer with the DC Bias Compensation Function

In Section 4, the design of the transformer was carried out. This section will carry out simulation research on the transformer.
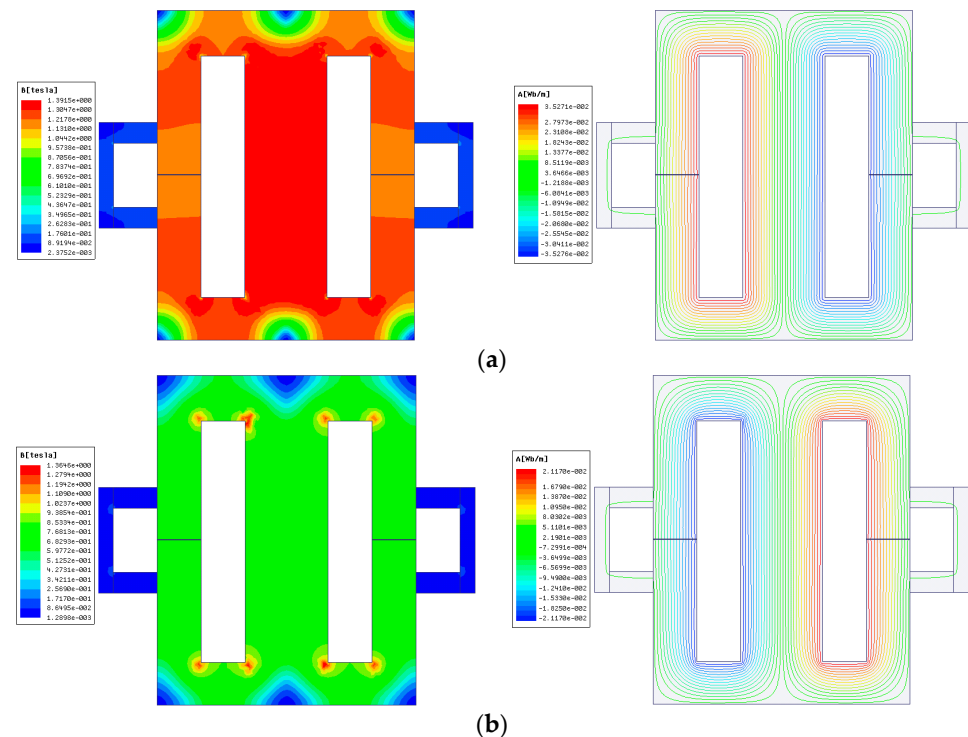
5.1. Simulation of the New Transformer with the DC Bias Compensation Function

Figure 11 shows the magnetic field distribution of the new transformer without DC bias.

Figure 12 shows the magnetic field distribution of the new transformer when the DC bias is 0.3 A. When the DC bias is 0.3 A, the magnetic density of the positive half cycle and the negative half cycle is not equal. The magnetic density of the positive half-cycle is about 1.3 T, and the magnetic density of the negative half-cycle is about 0.85 T.
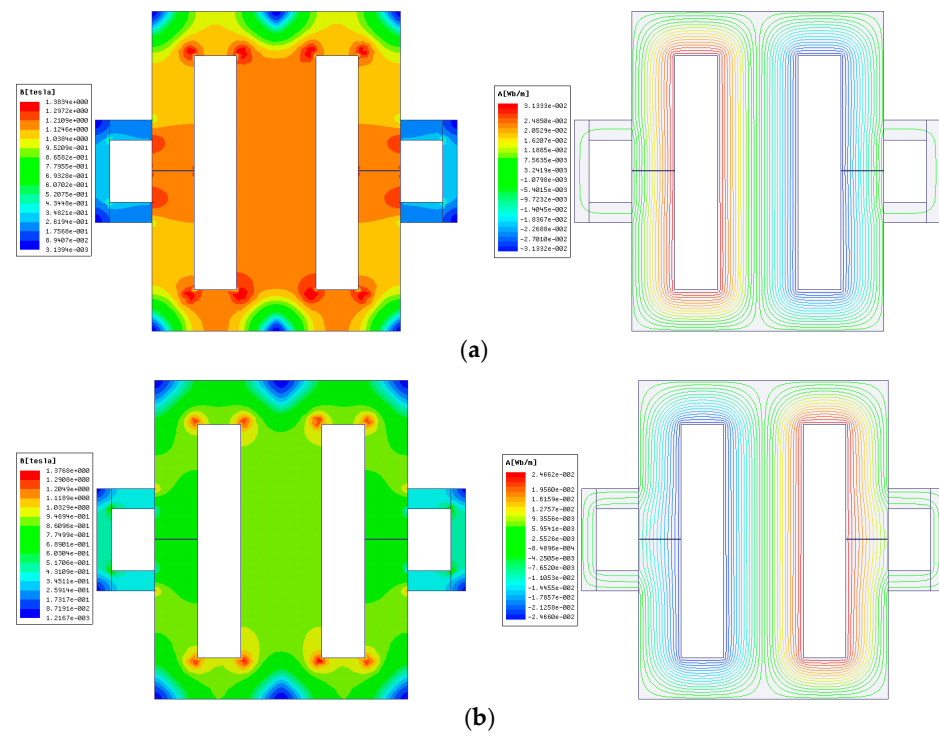
Figure 11. Magnetic field distribution of the new transformer without DC bias: (**a**) positive half-cycle and (**b**) negative half-cycle.
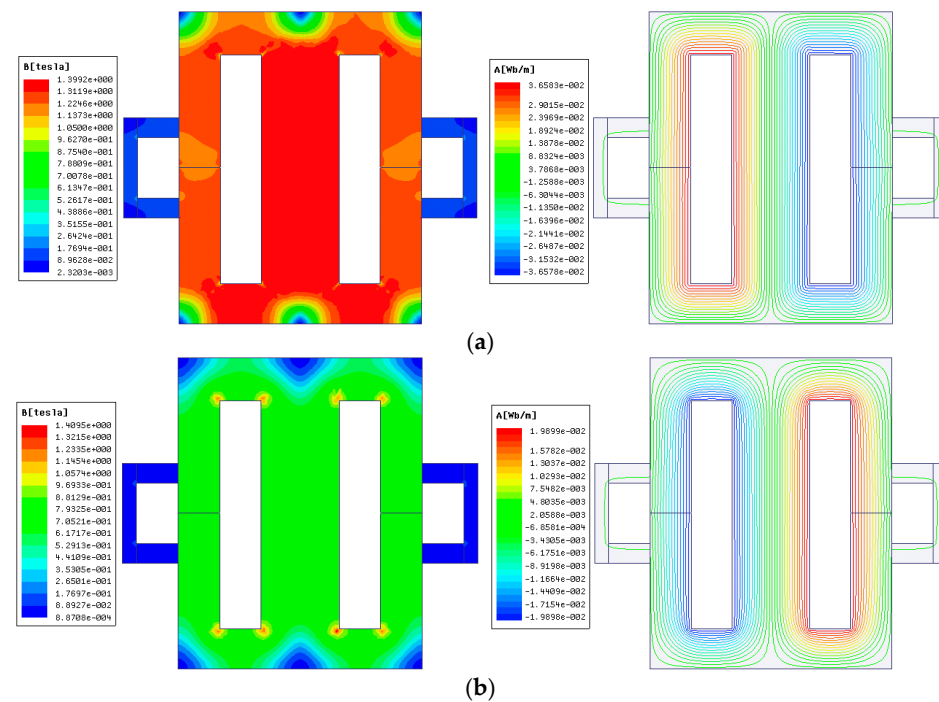

Figure 12. Magnetic field distribution of the new transformer when the DC bias is 0.3 A: (**a**) positive half-cycle and (**b**) negative half-cycle.

Figure 13 shows the magnetic field distribution of the new transformer after compensation when the DC bias is 0.3 A. After compensation, the magnetic densities of the positive half-cycle and the negative half-cycle are close to each other. The magnetic density of the positive half-cycle is about 1.21 T, and the magnetic density of the negative half-cycle is about 0.86 T.
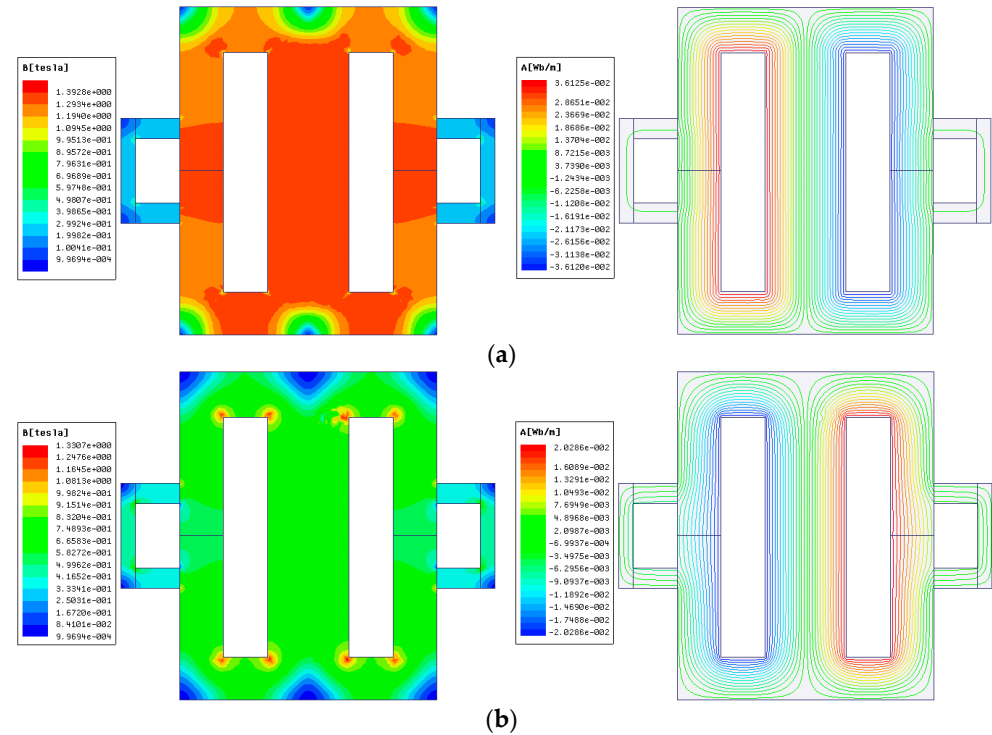
Figure 13. Magnetic field distribution of the new transformer after compensation when the DC bias is 0.3 A: (**a**) positive half-cycle and (**b**) negative half-cycle.

Figure 14 shows the magnetic field distribution of the new transformer when the DC bias is 0.6 A. When the DC bias is 0.6 A, the magnetic densities of the positive half-cycle and the negative half-cycle are not equal. The magnetic density of the positive half-cycle is about 1.38 T, and the magnetic density of the negative half-cycle is about 0.79 T.

Figure 14. Magnetic field distribution of the new transformer when the DC bias is 0.6 A: (**a**) positive half-cycle and (**b**) negative half-cycle.

Figure 15 shows the magnetic field distribution of the new transformer after compensation when the DC bias is 0.6 A. After compensation, the magnetic density of the positive half-cycle is about 1.32 T, and about 0.83 T in the negative half-cycle.

(**a**)

(**b**)

Figure 15. Magnetic field distribution of the new transformer after compensation when the DC bias is 0.6 A: (**a**) positive half-cycle and (**b**) negative half-cycle.

5.2. Experiment Simulation of the New Transformer with the DC Bias Compensation Function

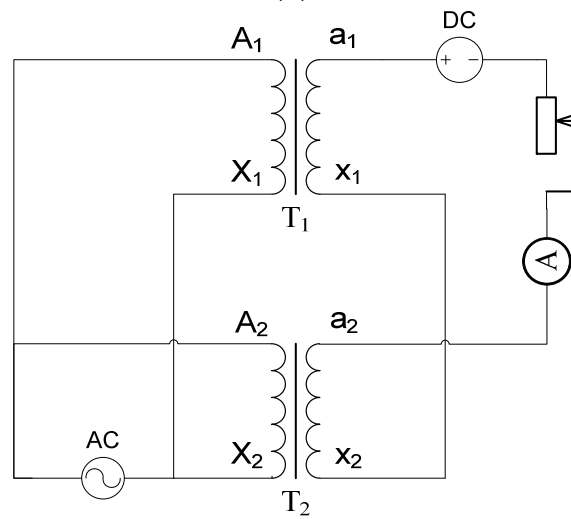The experimental site and experimental circuit diagram are shown in Figure 16.

Figure 17 is the excitation current waveform before and after the new transformer compensation when the bias current is 0.3 A. Figure 18 shows the excitation current waveform before and after the compensation of the new transformer when the bias current is 0.6 A.

The analysis indicates that the new transformer demonstrates effective compensation for bias current. When the DC bias phenomenon occurs, the positive peak of the excitation current increases, the negative peak decreases, and the working point of the transformer exciting current increases. When the bias current is compensated, the positive peak of the excitation current decreases and the negative peak increases. This compensation mechanism significantly contributes to addressing transformer faults caused by DC bias, aligning with the system design requirements.
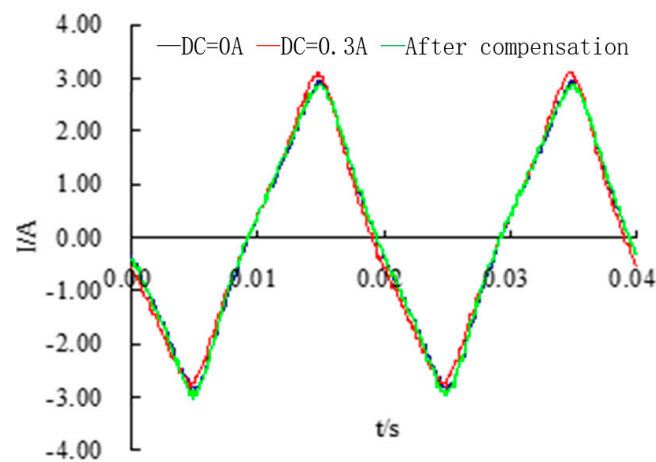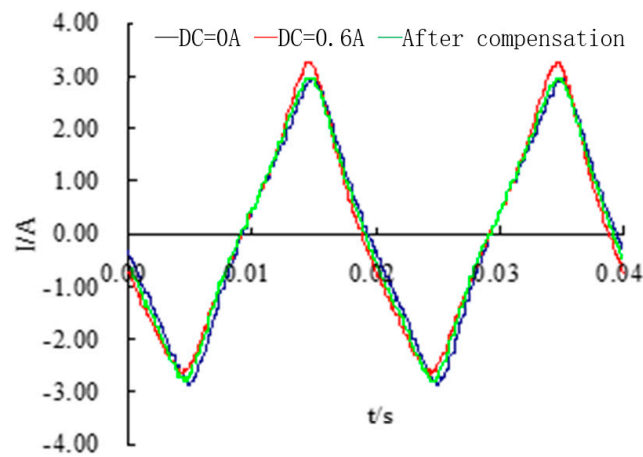
(**a**)

(**b**)

Figure 16. The experimental site and experimental circuit diagram: (**a**) experimental site and (**b**) experimental circuit diagram.

Figure 17. The excitation current waveform before and after the new transformer compensation when the bias current is 0.3 A.

Figure 18. The excitation current waveform before and after the new transformer compensation when the bias current is 0.6 A.

6. Conclusions

Based on the dual-phase hysteresis mathematical model, preparation, structure, and electromagnetic design of dual-phase magnetic materials, and simulation and experiments, a new type of transformer was designed and analyzed in detail. The conclusions are as follows:

(1) Based on the theory of micromagnetism, a hysteresis model of nano dual-phase composite magnetic materials was established using the OOMMF software platform and the micromagnetic simulation dynamic calculation method. The hysteresis loops of nano dual-phase composite magnetic materials under different soft magnetic layer thicknesses were calculated, and the relationship between soft magnetic layer thickness and coercivity was obtained.

(2) The structure of the transformer was designed and used for simulation verification. The simulation results show that when DC bias occurs, almost all of the compensating magnetic flux of the compensating iron core passes through the main magnetic circuit of the transformer, canceling out the DC magnetic flux in the main magnetic circuit and achieving the goal of eliminating DC bias, and the working magnetic flux of the transformer does not demagnetize the compensating iron core. When there is no DC bias, the compensating iron core has no residual magnetism, and the magnetic circuit of the compensating iron core does not affect the normal operation of the transformer. This proves the feasibility of the voltage regulator structure.

(3)   A 2 kVA power transformer prototype was developed, and experiments were conducted on the prototype. The experimental results show that under different DC bias conditions, after compensating for DC bias, the excitation current waveform of the transformer tends to be symmetrical. The positive peak value decreases and the negative peak value increases. The positive half-cycle magnetic flux density decreases, the iron core returns to an unsaturated state, and the negative half-cycle magnetic flux density increases, proving the suppression effect of the power transformer on DC bias.

The simulation and experimental results prove that the structure of the power transformer is reasonable, the DC bias suppression method is feasible, and it has a good suppression effect on DC bias. It realizes the automatic suppression of DC bias by the transformer itself, contributing to further research and solution of DC bias problems.

Author Contributions: Conceptualization, Y.L. and F.Y.; methodology, Y.H.; validation, J.G.; formal analysis, D.C.; investigation, Y.L.; resources, F.Y. and Y.H.; data curation, D.C. and H.B.; writing—original draft preparation, F.Y.; writing—review and editing, Y.L.; visualization, H.B.; funding acquisition, J.G. All authors have read and agreed to the published version of the manuscript.

Data Availability Statement: The raw data supporting the conclusions of this article will be made available by the authors on request.

Conflicts of Interest: Authors Yang Liu, Fuyao Yang, Yu Han and Jie Gao were employed by the State Grid Smart Grid Research Institute Co., Ltd. The remaining authors declare that the research was conducted in the absence of any commercial or financial relationships that could be construed as a potential conflict of interest.

References

1.   Cheng, S.; Cai, Z. Design and optimization of energy-saving wind power grid-connected contactor based on nano two-phase composite magnetic materials. In Proceedings of the 2017 4th International Conference on Electric Power Equipment-Switching Technology (ICEPE-ST), Xi'an, China, 22–25 October 2017; pp. 209–212.

2.   Kharitonskii, P.V.; Kosterov, A.A.; Gurylev, A.K.; Gareev, K.G.; Kirillova, S.A.; Zolotov, N.A.; Anikieva, Y.A. Magnetic States of Two-Phase Synthesized Fe_mO_n–$Fe_{3-x}Ti_xO_4$ Particles: Experimental and Theoretical Analysis. *Phys. Solid State* **2020**, *62*, 1691–1694. [CrossRef]

3.   Kharitonskii, P.V.; Gareev, K.G.; Ralin, A.Y.; Sergienko, E.S. Superparamagnetism of Fe_3O_4–$Fe_{3-x}Ti_xO_4$ Composites: Micromagnetic Modeling. *Phys. Metals Metallogr.* **2023**, *124*, 46–52. [CrossRef]

4.   Kramer, N.; Provino, A.; Hanley, C.; Kubiak, C.; Pathak, A.K. Magnetic properties of $LaFe_{2-x}Co_xSi$: A new two-phase naturally formed composite alloy. *AIP Adv.* **2023**, *13*, 025320. [CrossRef]

5.   Feng, H.; Wang, K.; Li, J.; Zhang, S.; Xie, Q.; Hu, X.; Li, B.; Wang, S.; Wang, S. Analysis of Exciting Current for Single-phase Four-Limb Ultra-High Voltage Transformer under DC Bias. In Proceedings of the 2018 Condition Monitoring and Diagnosis (CMD), Perth, WA, Australia, 23–26 September 2018; pp. 1–6.

6.   Cai, Y.; Yu, Q.; Guo, M.; Sun, G.; Sun, Q. Effect of heat treatments on the microstructure and magnetic properties of semi-hard magnetic 2J85 alloy. *J. Magn. Mater. Devices* **2013**, *1*, 47–51.

7.   Chapman, S.J. *Electric Machinery Fundamentals*; Publishing House of Electronics Industry: Beijing, China, 2012; pp. 1–30.

8.   Zhu, L.; Wei, C.; Yu, Y. Analysis of DC bias exciting current of the single-phase transformer and its effect on protection. *Power Syst. Prot. Control* **2010**, *38*, 158–162.

9.   Bolduc, L.; Granger, M.; Pare, G.; Saintonge, J.; Brophy, L. Development of a DC current-blocking device for transformer neutrals. *IEEE Trans. Power Deliv.* **2005**, *20*, 163–168. [CrossRef]

10.   Rajapakse, A.; Perera, N.; Faxvog, F.R.; Jensen, W.; Nordling, G.; Fuchs, G.; Jackson, D.B.; Volkmann, T.L.; Ruehl, N.; Groh, B. Power grid stability protection against GIC using a capacitive grounding circuit. In *PES T&D*; IEEE: Piscataway, NJ, USA, 2012; pp. 1–6.

11.   Hongtao, R. Analysis on Withstand Voltage of DC bias Device at 500kV Transformer Neutral Point. In Proceedings of the 2020 3rd International Conference on Power and Energy Applications (ICPEA), Busan, Republic of Korea, 9–11 October 2020; pp. 58–62.

12.   Li, C.; Zhang, Y.; Lv, Y.; Sun, S. Research on the design and experiment of power transformer DC bias blocking device. In Proceedings of the 2012 2nd International Conference on Consumer Electronics, Communications and Networks (CECNet), Yichang, China, 21–23 April 2012; pp. 2811–2814.

13. Lasabi, O.; Swanson, A.; Jarvis, L. Heuristic Control of Neutral DC Compensation Method to Moderate DC bias in Power Transformer. In Proceedings of the 2022 IEEE PES/IAS PowerAfrica, Kigali, Rwanda, 22–26 August 2022; pp. 1–5.
14. Pan, Z.; Wang, X.; Tan, B.; Zhu, L.; Liu, Y.; Liu, Y.; Wen, X. Potential compensation method for restraining the DC bias of transformers during HVDC monopolar operation. *IEEE Trans. Power Deliv.* **2015**, *31*, 103–111. [CrossRef]
15. Bachinger, F.; Hackl, A.; Hamberger, P.; Leikermoser, A.; Leber, G.; Passath, H.; Stoessl, M. Direct current in transformers: Effects and compensation. *E&I Elektrotechnik Informationstechnik* **2013**, 1–5. [CrossRef]
16. Fei, X.; Zhiwei, C.; Linzi, D.; Linjia, H.; Chen, J.; Gang, W. DC Bias Suppression Scheme Based on Hybrid Transformer. In Proceedings of the 2022 25th International Conference on Electrical Machines and Systems (ICEMS), Chiang Mai, Thailand, 29 November–2 December 2022; pp. 1–5.
17. Zhang, X.; Wu, W. Simulation analysis of converter transformer excitation current and reactive power loss in DC bias based on field circuit coupling. In Proceedings of the 2018 IEEE 4th Information Technology and Mechatronics Engineering Conference (ITOEC), Chongqing, China, 14–16 December 2018; pp. 861–864.
18. Ni, Y.; Zeng, X.; Yu, K.; Sun, S.; Zhuo, C.; Peng, P.; Su, Z. Modeling calculation and influence analysis of transformer DC bias current caused by metro stray current. In Proceedings of the 2021 IEEE 4th International Electrical and Energy Conference (CIEEC), Wuhan, China, 28–30 May 2021; pp. 1–6.
19. Zhao, J.; Fu, H.; Li, J.; Liu, Y.; Li, Z.; Pan, Z. The DC Bias Risk Assessment of Transformer Based on Nonlinear Magnetic Circuit Equations. In Proceedings of the 2019 IEEE 3rd Conference on Energy Internet and Energy System Integration (EI2), Changsha, China, 8–10 November 2019; pp. 2177–2181.
20. Yan, X.; Dong, X.; Han, G.; Yin, X.; Yu, X.; Jiao, Z.; Wang, X. Study of Transformer Loss and Temperature Rise Under DC Bias Magnetism Based on Finite Element Method. In Proceedings of the 2023 IEEE/IAS Industrial and Commercial Power System Asia (I&CPS Asia), Chongqing, China, 14–16 July 2023; pp. 429–434.
21. Subramanya, K.; Chelliah, T.R. Thermo Electrical Analysis and its Correlation in a DC Biased Power Transformer Subjected to Over and Under Excitations. In Proceedings of the 2023 13th International Conference on Power, Energy and Electrical Engineering (CPEEE), Tokyo, Japan, 25–27 February 2023; pp. 106–111.
22. Wang, G.; Zhang, G.; Liu, H.; Yu, D.; Wang, Q.; Chen, L. Analysis of the Influence of Transformer Harmonics Caused by DC Bias on Reactive Power Compensation Capacitor Banks. In Proceedings of the 2022 IEEE 5th International Electrical and Energy Conference (CIEEC), Nangjing, China, 27–29 May 2022; pp. 4576–4581.
23. Zheng, Y.; Pan, S.; Xia, Y.; Ouyang, X.; Shang, H.; Zhou, Q. Analysis on the Influence of the DC bias on spatial magnetic flux leakage in the transformer. In Proceedings of the 2022 IEEE International Conference on High Voltage Engineering and Applications (ICHVE), Chongqing, China, 25–29 September 2022; pp. 1–4.
24. Zhou, Z.; Hui, X.; Zhu, X.; Zhu, Y.; Xia, R. Research Summary on Transformer DC Magnetic Bias and Suppression Technology. In Proceedings of the 2023 8th Asia Conference on Power and Electrical Engineering (ACPEE), Tianjin, China, 14–16 April 2023; pp. 2715–2719.
25. Zheng, L.; Su, K.; Liu, X.; Zhao, J.; Guo, H.; Xun, H. Analysis of DC Magnetic Bias Influences on Transformers. In Proceedings of the 2020 IEEE 4th Conference on Energy Internet and Energy System Integration (EI2), Wuhan, China, 30 October–1 November 2020; pp. 3329–3332.
26. Chikazumi, S. *Physics of Ferromagnetism*; Oxford University Press: New York, NY, USA, 1997.